JPE 18-3-16

https://doi.org/10.6113/JPE.2018.18.3.817
ISSN(Print): 1598-2092 / ISSN(Online): 2093-4718

Generalized Vector Control with Reactive Power Control for Brushless Doubly-Fed Induction Machines

Qiwei Duan[†], Shi Liu[*], H. Inaki Schlaberg[*], and Teng Long[**]

[†,*]School of Energy, Power and Mechanical Engineering, North China Electric Power University, Beijing, China
[**]Department of Engineering, University of Cambridge, Cambridge, ENG, UK

Abstract

In this paper, a current hysteresis control with good decoupling properties for doubly-fed brushless induction machines (BDFIMs) has been proposed based on a generalized vector model. The independent control of the reactive power and speed for BDFIMs has been achieved by controlling the d-axis and the q-axis current of the control windings (CW). The proposed vector control method has been developed for the power winding (PW) flux frame. Experimental verification of a type Y180M-4 BDFIM prototype with 1/4 pole-pairs has been presented. Evidence of its good performance has been shown through experimental results.

Key words: Brushless doubly-fed induction machine, Current hysteresis control, Electromagnetic torque expression, Four-quadrant power converter, Generalized vector model, PI controller, Speed control

NOMENCLATURE

ω_1, ω_2	Angular frequencies of the supplies to the power winding and control winding
p_1, p_2	Pole-pairs of the power winding and control winding
$\boldsymbol{v}_{s1}, \boldsymbol{v}_{s2}, \boldsymbol{v}_r$	Voltage matrix for the power winding, control winding and rotor
$\boldsymbol{i}_{s1}, \boldsymbol{i}_{s2}, \boldsymbol{i}_r$	Current matrix for the power winding, control winding and rotor
$\boldsymbol{\lambda}_{s1}, \boldsymbol{\lambda}_{s2}, \boldsymbol{\lambda}_r$	Flux matrix for the power winding, control winding and rotor
$\boldsymbol{R}_{s1}, \boldsymbol{R}_{s2}, \boldsymbol{R}_r$	Resistance matrix for the power winding, control winding and rotor
$\boldsymbol{M}_{s1}, \boldsymbol{M}_{s2}, \boldsymbol{M}_r$	Inductance matrix for the power winding, control winding and rotor
$\boldsymbol{M}_{s1r}, \boldsymbol{M}_{s2r}$	Mutual inductance matrix for the power winding and control winding
L_1, L_2	Self-inductances of the power winding and control winding
L_{l1}, L_{l2}	Leakage inductances of the power windings and control windings
$\bar{\boldsymbol{V}}, \bar{\boldsymbol{I}}, \bar{\boldsymbol{\Lambda}}, \boldsymbol{R}$	Voltage, current, flux vector and resistance
$\theta_{s1}, \theta_{s2}, \varphi_r$	Position angle of the reference frame for the power winding, control winding and rotor
ω_{s1}, ω_{s2}	Differential values of θ_{s1}, θ_{s2}
$real\{\}$	Real part of a vector
X^*	Complex conjugate of vector X
X^t	Transpose of matrix X
d/dt	Differential sign
T_e	The electromagnetic torque of a BDFIM

SUBSCRIPTS

s_1, s_2, r	Variables of the power winding, control winding and rotor

Manuscript received Mar. 2, 2017; accepted Mar. 14, 2018
Recommended for publication by Associate Editor Yong Kang.
[†]Corresponding Author: dqwforfly@163.com
Tel: +86-10-61773377, North China Electric Power University
[*]School of Energy, Power and Mechanical Engineering, North China Electric Power University, China
[**]Department of Engineering, University of Cambridge, UK

I. INTRODUCTION

These days, renewable power generation, especially wind power generation, is receiving a lot of attention due to its

environmental friendliness. BDFIMs are being widely applied in offshore wind power and large scale wind power generation systems. A BDFIM has two three-phase windings, a power winding (PW) that a directly connected to the grid, and a control winding (CW) that is connected to the grid by a back-to-back PWM converter. To avoid direct electromagnetic cross-coupling between the two stators, the pole number for the two stators is different. The rotor is designed to couple to the two stators where the number of the nests is equal to the pole-pairs of the two stators.

Many control strategies for BDFIMs have been proposed in recent years, such as direct power control [1], direct torque control (DTC) [2] and indirect stator-quantities control (ISC) [3]. Of these strategies, the vector control (VC), i.e. the field/voltage-orientation control strategy, which has been successfully applied to doubly-fed induction machines (DFIMs) [4]-[6], has the largest number of control strategies for BDFMs, resulting in better dynamic performance[7]-[10]. To study control strategies, a relatively precise mathematical model for a BDFIM is required to predict its dynamic and steady-state performances.

A detailed mathematical model of a BDFIM, where the real rotor structure was taken care of, was first proposed in [11]. After that, a two-axis models was proposed by Wallace [12]. Based on the two-axes model, a simplified control method for BDFMs was proposed, were the controller is aligned with the rotor flux [13]. Roberts developed a coupled-circuit model for a wide range of BDFMs including the BDFIM [14]. The parameter values calculated in the coupled-circuit model can be used in other models. However, the coupled-circuit model is too complex to be used to analyse control strategies. A unified reference frame d-q model for BDFMs was proposed by Poza et al [15] for BDFMs with a nested-loop rotor with one loop in each nest. They also developed a new vector control method in which both the reactive power and speed can be controlled [16]. However, the calculation of the compensation module is complex. Subsequently, Shao proposed a PW-flux-oriented control based on a unified reference frame d-q model for a BDFIM [10], [17]. This method allows for the control of the speed and reactive power. However, compensation for the two control loops is missing. Thus, the speed and reactive power control loop have a strong coupling effect. Farhad proposed a generalized vector model for BDFIMs that can be generalized to BDFIMs with any number of loops per nest [18]. In addition, the effects of all the loops per nest are taken into account. It then presented a generalized vector control with a speed control loop but without a reactive power controller.

In this paper, a speed control strategy is proposed based on the generalized vector torque equation. Then a reactive power control loop is established. The control scheme has better decoupling performance than other PW−flux−oriented vector control schemes such as those presented in [10], [17]. A detailed theoretical derivation of the generalized vector control method is presented.

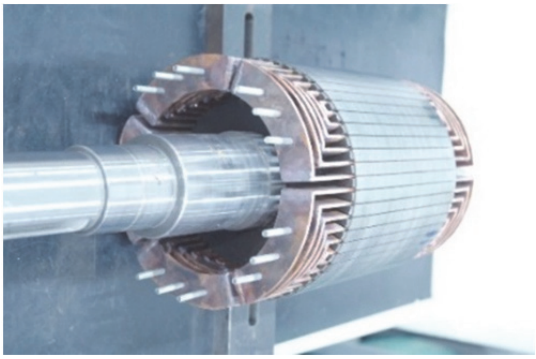

Fig. 1. Rotor of the BDFIM prototype.

In the existing literature, there is no effective expression for the torque for a BDFIM to facilitate the analysis of control strategies. This paper attempts to fill this void by presenting two concise electromagnetic torque equations that are similar to the electromagnetic torque equations of doubly fed induction machines (DFIM), where the modelling and control methods are already very mature.

In order to demonstrate the control performance of the proposed controller, a four-quadrant PWM converter control system is constructed. The good control and decoupling performances of the current hysteresis control strategy are shown in experimental results.

II. Generalized Vector Model for the BDFIM

The rotor angular frequency of a BDFIM operated in the synchronous (doubly fed) mode is given as follows:

$$\omega_r = \frac{\omega_1 \pm \omega_2}{p_1 + p_2} \tag{1}$$

Where ω_r is the rotor shaft speed, the "+" indicates that the BDFIM is operated at super-synchronous speeds, and the "-" indicates that the BDFIM is operated at sub-synchronous speeds.

The BDFIM coupled-circuit equations are as follows [18]:

$$\begin{cases} \boldsymbol{v}_{s1} = \boldsymbol{R}_{s1}\boldsymbol{i}_{s1} + \dfrac{d\lambda_{s1}}{dt} \\ \boldsymbol{v}_{s2} = \boldsymbol{R}_{s2}\boldsymbol{i}_{s2} + \dfrac{d\lambda_{s2}}{dt} \\ \boldsymbol{v}_r = \boldsymbol{R}_r\boldsymbol{i}_r + \dfrac{d\lambda_r}{dt} \end{cases} \tag{2}$$

$$\begin{cases} \lambda_{s1} = \boldsymbol{M}_{s1}\boldsymbol{i}_{s1} + \boldsymbol{M}_{s1r}\boldsymbol{i}_r \\ \lambda_{s2} = \boldsymbol{M}_{s2}\boldsymbol{i}_{s2} + \boldsymbol{M}_{s2r}\boldsymbol{i}_r \\ \lambda_r = \boldsymbol{M}_{s1r}^T\boldsymbol{i}_{s1} + \boldsymbol{M}_{s2r}^T\boldsymbol{i}_{s2} + \boldsymbol{M}_r\boldsymbol{i}_r \end{cases} \tag{3}$$

$$\begin{cases} T_e = [\boldsymbol{i}_{s1}^T \ \boldsymbol{i}_{s2}^T]\begin{bmatrix} \frac{d\boldsymbol{M}_{s1r}}{d\theta_r} \\ \frac{d\boldsymbol{M}_{s2r}}{d\theta_r} \end{bmatrix}\boldsymbol{i}_r \\ J\dfrac{d\omega_r}{dt} = T_e - T_l \\ \omega_r = \dfrac{d\theta_r}{dt} \end{cases} \tag{4}$$

Where T_e and T_l are the electromagnetic and load torques, respectively. θ_r is the rotor position angle. J is the rotor moment of inertia.

The BDFIM coupled-circuit model can accurately predict the transient performance of the machine and it includes the effects of all the space-harmonic components of the inductance parameters. However, the order of the model is too high to analyze and design a control system. Therefore, a generalized vector model is created to analyze and design a control system more conveniently based on the transform equations (5) [18]:

$$\begin{cases} \overline{\boldsymbol{F}}_{s1} = \dfrac{2}{3}[1, \boldsymbol{e}^{j\frac{2}{3}\pi}, \boldsymbol{e}^{-j\frac{2}{3}\pi}]\boldsymbol{f}_{s1} \\ \overline{\boldsymbol{F}}_{s2} = \dfrac{2}{3}[1, \boldsymbol{e}^{j\frac{2}{3}\pi}, \boldsymbol{e}^{-j\frac{2}{3}\pi}]\boldsymbol{f}_{s2} \\ \overline{\boldsymbol{F}}_r = \dfrac{1}{3}[\overline{\boldsymbol{E}}_{N\times N}, \overline{\boldsymbol{E}}_{N\times N}\boldsymbol{e}^{j\frac{2\pi p_1}{S}}, \\ \overline{\boldsymbol{E}}_{N\times N}\boldsymbol{e}^{j\frac{2\pi 2p_1}{S}}, \cdots, \overline{\boldsymbol{E}}_{N\times N}\boldsymbol{e}^{j\frac{2\pi(S-1)p_1}{S}}]\boldsymbol{f}_r \end{cases} \tag{5}$$

Where $\overline{\boldsymbol{F}}_{s1}, \overline{\boldsymbol{F}}_{s2}, \overline{\boldsymbol{F}}_r$ indicate the PW, CW and rotor quantities under the generalized vector model; $\boldsymbol{f}_{s1}, \boldsymbol{f}_{s2}, \boldsymbol{f}_r$ indicate the PW, CW and rotor quantities under the abc frame (coupled-circuit model).

By means of the vector transformation equations (5) for coupled-circuit equations, the generalized vector model of the BDFIM can be expressed as [19]:

$$\overline{\boldsymbol{V}}_{s1} = R_1\overline{\boldsymbol{I}}_{s1} + \frac{d\overline{\boldsymbol{\Lambda}}_{s1}}{dt} - j\omega_{s1}\overline{\boldsymbol{\Lambda}}_{s1} \tag{6}$$

$$\overline{\boldsymbol{V}}_{s2} = R_2\overline{\boldsymbol{I}}_{s2} + \frac{d\overline{\boldsymbol{\Lambda}}_{s2}}{dt} - j\omega_{s2}\overline{\boldsymbol{\Lambda}}_{s2} \tag{7}$$

$$0 = \overline{\boldsymbol{V}}_r = \overline{\boldsymbol{R}}_r\overline{\boldsymbol{I}}_r + \frac{d\overline{\boldsymbol{\Lambda}}_r}{dt} - jp_1(\frac{d\varphi_r}{dt})\overline{\boldsymbol{\Lambda}}_r \tag{8}$$

$$\overline{\boldsymbol{\Lambda}}_{s1} = (L_{l1} + \frac{3}{2}L_1)\overline{\boldsymbol{I}}_{s1} + 3\overline{\boldsymbol{M}}_{s1r}e^{-j\eta}\overline{\boldsymbol{I}}_r \tag{9}$$

$$\overline{\boldsymbol{\Lambda}}_{s2} = (L_{l2} + \frac{3}{2}L_2)\overline{\boldsymbol{I}}_{s2} + 3\overline{\boldsymbol{M}}_{s2r}e^{j\gamma}\overline{\boldsymbol{I}}_r^* \tag{10}$$

$$\begin{aligned} \overline{\boldsymbol{\Lambda}}_r = (\overline{\boldsymbol{L}}_r - \overline{\boldsymbol{M}}_r)\overline{\boldsymbol{I}}_r + \frac{3}{2}\overline{\boldsymbol{M}}_{s1r}^t e^{j\eta}\overline{\boldsymbol{I}}_{s1} \\ + \frac{3}{2}\overline{\boldsymbol{M}}_{s2r}^t e^{j\gamma}\overline{\boldsymbol{I}}_{s2}^* \end{aligned} \tag{11}$$

$$\begin{aligned} T_e = & \frac{9}{2}p_1\overline{\boldsymbol{M}}_{s1r}real\{\overline{\boldsymbol{I}}_r\overline{\boldsymbol{I}}_{s1}^* e^{j(\frac{\pi}{2}-\eta)}\} \\ & + \frac{9}{2}p_2\overline{\boldsymbol{M}}_{s2r}real\{\overline{\boldsymbol{I}}_r\overline{\boldsymbol{I}}_{s2}^* e^{j(\frac{\pi}{2}+\gamma)}\} \end{aligned} \tag{12}$$

Where the free variables η and γ are given as:

$$\eta = p_1\varphi_r - \theta_{s1} - p_1\theta_r \tag{13}$$

$$\gamma = p_1\varphi_r + \theta_{s2} + p_2(\theta_r - \zeta) \tag{14}$$

The model can be used in a p_1/p_2 pole-pair BDFIM with a nested-loop that has N loops per nest. Where $\overline{\boldsymbol{R}}_r \in R^{N\times N}$ is the nest resistance matrix (from the inner loop to the outer loop). $\overline{\boldsymbol{M}}_{s1r} \in R^{1\times N}, \overline{\boldsymbol{M}}_{s2r} \in R^{1\times N}$ are the mutual inductance matrices for the PW-Rotor and CW-Rotor, respectively. $\overline{\boldsymbol{L}}_r \in R^{N\times N}, \overline{\boldsymbol{M}}_r \in R^{N\times N}$ are the nest inductance matrix and the mutual inductances, respectively. ζ is the physical displacement angle between the PW and the CW.

III. Vector Control Method

A. Selection of $\varphi_r, \theta_{s1}, \theta_{s2}$ Based on the PW-flux-oriented Frame

As can be seen in the generalized vector model, the free variables η and γ can be given as arbitrary values. In this paper the values of η and γ are given as zero to make the time-varying terms in equations (9), (10), (11) and (12) constants.

Based on the PW-flux-oriented control method, the reference angle of the PW variables can be given as:

$$\theta_{s1} = -\theta_{\overline{\Lambda}_{s1}} \tag{15}$$

Where, $\theta_{\overline{\Lambda}_{s1}}$ is the angular position of the PW flux vector.

Then based on (13), (14) and (15), θ_{s2} and φ_r can be expressed as:

$$\begin{cases} \theta_{s2} = \theta_{\overline{\Lambda}_{s1}} - (p_1 + p_2)\theta_r + p_2\zeta \\ \varphi_r = \dfrac{1}{p_1}(p_1\theta_r - \theta_{\overline{\Lambda}_{s1}}) \end{cases} \tag{16}$$

The magnitudes of ω_{s1} and ω_{s2} can be expressed as:

$$\begin{cases} \omega_{s1} = -\omega_1 \\ \omega_{s2} = \omega_1 - (p_1 + p_2)\omega_r \end{cases} \tag{17}$$

The identification of the parameters for the rotating reference frame for the PW and CW is shown in Fig. 2. As can be seen in this figure, the magnitude of ζ is $\pi/4$, i.e. the position angle between the PW and CW.

The PW flux-linkage of two components in the stationary reference frame is given as follows [14]:

$$\begin{cases} \overline{\boldsymbol{\Lambda}}_{s1\alpha} = \int(\overline{\boldsymbol{V}}_{s1\alpha} - R_1\overline{\boldsymbol{I}}_{s1\alpha})dt \\ \overline{\boldsymbol{\Lambda}}_{s1\beta} = \int(\overline{\boldsymbol{V}}_{s1\beta} - R_1\overline{\boldsymbol{I}}_{s1\beta})dt \end{cases} \tag{18}$$

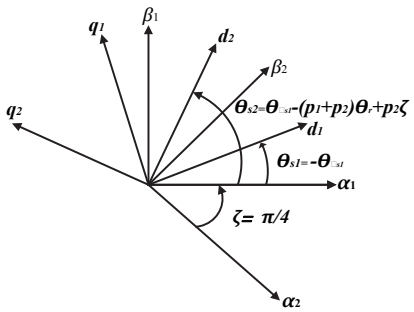

Fig. 2. Reference frame for the BDFIM.

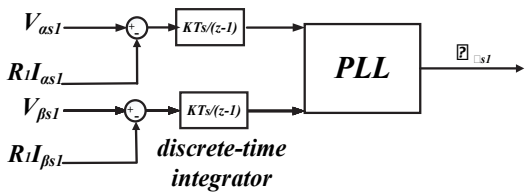

Fig. 3. PW flux angle estimation by the PLL technique.

Thus, the PW flux vector position angle $\theta_{\bar{\Lambda}s1}$ can be estimated by the PLL technique. A block diagram of the PW flux angle estimation technique of the control system is shown in Fig. 3. In discrete-time sampling systems, the transfer function of the integral part can be expressed as $KTs/(z-1)$, where K is the integral coefficient and T_s is the sampling time. The rotor position angle θ_r is obtained from an incremental encoder. Then θ_{s2} can be calculated by expression (16).

B. Expressions for $\bar{\Lambda}_r$, $\bar{I}_r$ and $\bar{I}_{s1}$

Since $\eta = \gamma = 0$, the BDFIM flux equations can be expressed as:

$$\begin{cases} \bar{\Lambda}_{s1} = (L_{l1} + \frac{3}{2}L_1)\bar{I}_{s1} + 3\bar{M}_{s1r}\bar{I}_r \\ \bar{\Lambda}_{s2} = (L_{l2} + \frac{3}{2}L_2)\bar{I}_{s2} + 3\bar{M}_{s2r}\bar{I}_r^* \\ \bar{\Lambda}_r = (\bar{L}_r - \bar{M}_r)\bar{I}_r + \frac{3}{2}\bar{M}_{s1r}^t\bar{I}_{s1} + \frac{3}{2}\bar{M}_{s2r}^t\bar{I}_{s2}^* \end{cases} \tag{19}$$

The electromagnetic torque equation can be expressed as:

$$T_e = \frac{9}{2}p_1\bar{M}_{s1r}real\{\bar{I}_r\bar{I}_{s1}^*j\} + \frac{9}{2}p_2\bar{M}_{s2r}real\{\bar{I}_r\bar{I}_{s2}^*j\} \tag{20}$$

Based on the rotor flux equation (19):

$$\begin{cases} \bar{I}_r = (\bar{L}_r - \bar{M}_r)^{-1}(\bar{\Lambda}_r - \frac{3}{2}\bar{M}_{s1r}\bar{I}_{s1} - \frac{3}{2}\bar{M}_{s2r}\bar{I}^*_{s2}) \\ \bar{I}_{s1} = \frac{1}{L}[\bar{\Lambda}_{s1} - 3\bar{M}_{s1r}(\bar{L}_r - \bar{M}_r)^{-1}\bar{\Lambda}_r + \frac{9}{2}\bar{M}_{s1r}(\bar{L}_r - \bar{M}_r)^{-1}\bar{M}_{s2r}^t\bar{I}_{s2}^*] \end{cases} \tag{21}$$

Where: $L = L_{l1} + \frac{3}{2}L_1 - \frac{9}{2}\bar{M}_{s1r}(\bar{L}_r - \bar{M}_r)^{-1}\bar{M}_{s1r}^t$.

Based on equation (21), $\bar{I}_{s2}^*$ can be expressed by the following two equations:

$$\begin{cases} \bar{I}_{s2}^* = \frac{2}{3}(\bar{M}_{s2r}^t)^{-1}[\bar{\Lambda}_r - \frac{3}{2}\bar{M}_{s1r}^t\bar{I}_{s1} - (\bar{L}_r - \bar{M}_r)\bar{I}_r] \\ \bar{I}_{s2}^* = \frac{2}{9\bar{M}_{s1r}(\bar{L}_r - \bar{M}_r)^{-1}\bar{M}_{s2r}^t}[L\bar{I}_{s1} - \bar{\Lambda}_{s1} + 3\bar{M}_{s1r}(\bar{L}_r - \bar{M}_r)^{-1}\bar{\Lambda}_r] \end{cases} \tag{22}$$

Where, $(\bar{M}_{s2r}^t)^{-1}$ is defined as $(\bar{M}_{s2r}^t)^{-1}\bar{M}_{s2r}^t = 1$.

Based on (21) and (22):

$$\begin{cases} \bar{I}_r = \bar{G}_1\bar{\Lambda}_r + \bar{G}_2\bar{\Lambda}_{s1} \\ \bar{\Lambda}_r = \bar{G}_3\bar{I}_r + \bar{G}_4\bar{\Lambda}_{s1} \end{cases} \tag{23}$$

Based on (19) and (23):

$$\begin{cases} \bar{I}_r = \bar{G}_i\bar{\Lambda}_{s1} \\ \bar{\Lambda}_r = \bar{G}_r\bar{\Lambda}_{s1} \\ \bar{I}_{s1} = G_s\bar{\Lambda}_{s1} \end{cases} \tag{24}$$

$\bar{G}_1, \bar{G}_2, \bar{G}_3, \bar{G}_4, \bar{G}_i, \bar{G}_r$ and G_s are shown in the Appendix.

It should be noted that $\bar{I}_{s1}$, $\bar{\Lambda}_r$ and $\bar{I}_r$ depend on $\bar{\Lambda}_{s1}$ as the coefficients $\bar{G}_i$, $\bar{G}_r$ and G_s. In addition they contain $\bar{M}_{s1r}, \bar{M}_{s2r}$, $\bar{L}_r$ and $\bar{M}_r$ which depend on the interactions between the two stator windings (PW and CW) and the rotor windings. In fact, the values of $\bar{I}_{s1}$, $\bar{\Lambda}_r$ and $\bar{I}_r$ mainly depend on the value of $\bar{\Lambda}_{s1}$, and are influenced by the electromagnetic interactions in the BDFIM.

C. Speed/Torque Control Loop

Substituting (19) and (24) into (20) yields:

$$T_{e1} = F_1\,\mathrm{Im}\{\bar{\Lambda}_{s1}\bar{\Lambda}_{s2}^*\} \tag{25}$$

Where: $F_1 = \frac{9P_2}{2G_c(L_{l2} + \frac{3}{2}L_2)}[3\bar{M}_{s2r}\bar{G}_i - G_c]\,\bar{M}_{s2r}\bar{G}_i$

Substituting (24) into (20) gives:

$$T_{e2} = F_2\,\mathrm{Im}\{\bar{I}_{s1}\bar{I}_{s2}^*\} \tag{26}$$

Where: $F_2 = -(9P_2/2G_s)\bar{M}_{s2r}\bar{G}_i$.

The electromagnetic torque equations (25) and (26) are similar to the electromagnetic torque equations of a DFIM [20]. These two equations can facilitate the modelling of the controller.

Substituting (24) into (26) yields:

$$T_e = G_sF_2\,\mathrm{Im}\{\bar{\Lambda}_{s1}\bar{I}_{s2}^*\} \tag{27}$$

The proposed controller is aligned with the PW flux reference frame. Therefore, $\bar{\Lambda}_{ds1} = \bar{\Lambda}_{s1} = |\bar{\Lambda}_{s1}|$ and $\bar{\Lambda}_{qs1} = 0$. Since the PW is directly connected to a 50 Hz, 220 V grid, a voltage frequency of ω_1 can be considered stable and the PW flux has a constant magnitude [17]. Then the electromagnetic torque can be expressed as:

$$T_e = G\bar{I}_{qs2} \tag{28}$$

Where, $G = -G_sF_2|\bar{\Lambda}_{s1}|$. Obviously, the coefficient G is constant.

Expression (28) shows that T_e can be directly controlled by $\bar{I}_{qs2}$.

The mechanical differential equation is:

$$T_e = J\frac{d\omega_r}{dt} + T_l = Js\omega_r + T_l \tag{29}$$

Where, J is the moment of inertia. As can be seen in (29), T_e has a first order linear relation with ω_r. Obviously, the speed of the machine can be controlled by $\bar{I}_{qs2}$.

D. Reactive Power Control Loop

The reactive power of the BDFIM can be expressed as [21]:

$$Q_p = \frac{3}{2}\mathrm{Im}\{\overline{\boldsymbol{V}}_{s1}\,\overline{\boldsymbol{I}}^{*}_{s1}\} \tag{30}$$

Since $\omega_{s1}=-\omega_1$, the PW voltage equation (6) can be expressed as:

$$\overline{\boldsymbol{V}}_{s1} = R_1\overline{\boldsymbol{I}}_{s1} + \frac{d\overline{\boldsymbol{\Lambda}}_{s1}}{dt} + j\omega_1\overline{\boldsymbol{\Lambda}}_{s1} \tag{31}$$

By substituting (21) and (23) into the reactive power expression (30):

$$Q_p = M\overline{\boldsymbol{I}}_{ds2} + Q_d \tag{32}$$

Where:

$$\begin{cases} M = \dfrac{27}{4L}\omega_1\left|\overline{\boldsymbol{\Lambda}}_{s1}\right|\overline{\boldsymbol{M}}_{s1r}(\overline{\boldsymbol{L}}_r - \overline{\boldsymbol{M}}_r)^{-1}\overline{\boldsymbol{M}}^{t}_{s2r} \\ Q_d = \dfrac{3}{2L}\omega_1\left|\overline{\boldsymbol{\Lambda}}_{s1}\right|^2[1 - 3\overline{\boldsymbol{M}}_{s1r}(\overline{\boldsymbol{L}}_r - \overline{\boldsymbol{M}}_r)^{-1}\overline{\boldsymbol{G}}_r] \end{cases}$$

Since M and Q_d remain fixed, Q_p and $\overline{I}_{qs2}$ have a fixed and a first order relationship. Then the reactive power of the BDFIM can be independently controlled by $\overline{I}_{ds2}$.

E. Proposed Control Strategy

A structural diagram of the vector control method is shown in Fig. 4. The reference outputs of the speed and reactive power control loops are $\overline{I}_{qs2,ref}$ and $\overline{I}_{ds2,ref}$. From here the three-phase stationary frame current $\overline{I}_{s2(abc)}$ is calculated with an inverse park transformation as the reference value of the hysteresis current controller. The machine side converter (MSC) receives switching signals generated by the hysteresis current controller. That is to say, the CW voltage can be controlled by the CW current [22]. Finally, the torque and reactive power can be controlled by $\overline{V}_{qs2}$ and $\overline{V}_{ds2}$, respectively [17].

IV. Experimental Verification

A BDFIM test rig is set up to validate the control algorithm as shown in Fig. 5. The parameters of the prototype BDFIM are listed in Table I. A DC machine was mechanically coupled to the prototype to act as a load machine. The speed signal and rotor position angle were obtained by an incremental encoder with a resolution of 1024 cycles/r. The CW was supplied by a back-to-back PWM converter, and the PW was connected to the grid (220 V, 50 Hz). The GSC and MSC of the back-to-back PWM converter were controlled by a digital signal processor (DSP, TMS320F28335). The sampling time of the controller was 0.3 ms.

A. Response to Speed Variation

Waveforms in the presence of trapezoidal speed variations are shown in Fig. 6. The experimental conditions are as follows. The reference rotating speed starts to vary from 600 r/min (synchronous speed) to 720 r/min (super-synchronous speed). Then it descends to 480 r/min (sub-synchronous speed) and finally increases to 600 r/min. The reference reactive power is 1400 var. The top two graphs in Fig. 6 demonstrate the excellent tracking of reference speeds in the

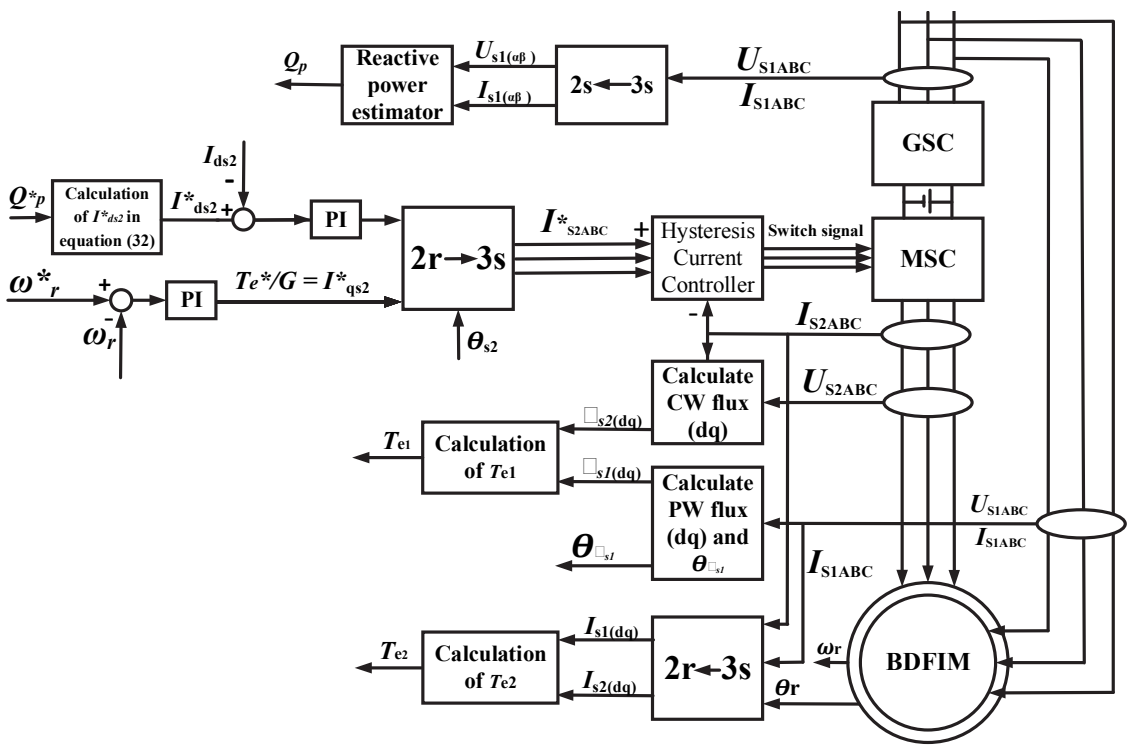

Fig. 4. Structural diagram of the vector control method.

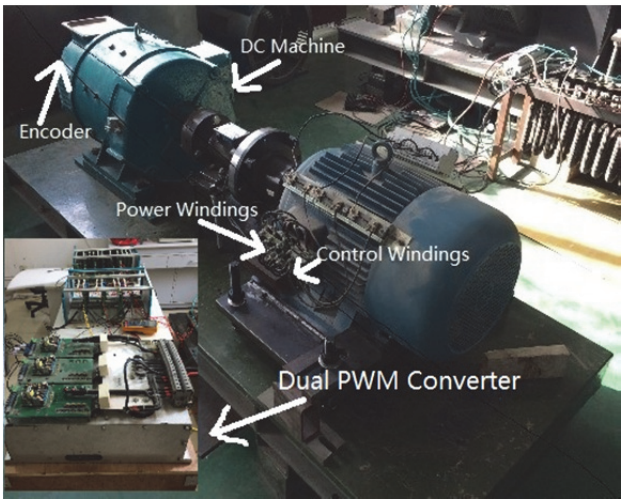

Fig. 5. Experimental platform.

TABLE I
PROTOTYPE PARAMETERS

Parameter	Value
Frame size	Y180M-4
PW pole -pairs	4
CW pole -pairs	1
Natural speed	600r/m
PW rated power	15kW at 50Hz
CW rated power	1.5kW at 50Hz
PW rated V,I	380V, 30A at 50Hz
CW rated V,I	40V, 13A at 5Hz
Rated torque	318 N·m
Numbers of loop	6

experimental process while the captured Q_p is only marginally affected. In fact, the reactive power of the machine can be kept relatively stable during speed variations. It is indicated that the coupling effect in the speed control loop, i.e., ω_r-Te-$\bar{I}_{qs2}$-$\bar{V}_{qs2}$ that has an impact on the reactive power control loop, i.e., Q_p-$\bar{I}_{ds2}$-$\bar{V}_{ds2}$ can be significantly reduced.

Three torque waveform signals T_{e1}, T_{e2} and T_e are shown in Fig. 6. It is evident that the values of T_{e1} and T_{e2}, which are calculated using the proposed torque expressions (25) and (26), are in accordance with the value of the measured torque T_e. The error is mostly due to approximations such as neglecting the iron loss and iron saturation of the generalized vector model, and the computing errors of the parameters. T_e is proportional to $\bar{I}_{qs2}$ as shown in Fig. 6 which demonstrates the reliability of expression (28).

B. Response to Load Torque Continuous Variations

Fig. 7 shows the good stability of the speed control and reactive power control when the load torque step changes from no-load to 140 N.m and then back down to no-load. The calculation of T_{e1} and T_{e2} agrees with the measured torque T_e. Another interesting observation is that the PW current increases significantly when the load torque increases gradually. In addition, this is done while the increase of the CW current is not obvious. This indicates that the PW plays a more prominent role in active power generation.

The obtained experimental results indicate that the coupling effect in the torque control loop, i.e., ω_r-Te-$\bar{I}_{qs2}$-$\bar{V}_{qs2}$ that impacts the reactive power control loop, i.e., Qp-$\bar{I}_{ds2}$-$\bar{V}_{ds2}$ can be significantly reduced.

C. Response to Reactive Power Variations

Fig. 8 shows the response of the machine to a step change in the reactive power while the speed is set to 674 r/min (super-synchronous speed) and the machine is in the no-load condition. The PW reactive power changes from +2000 var to -2000 var and then back to +2000 var. During the dynamic

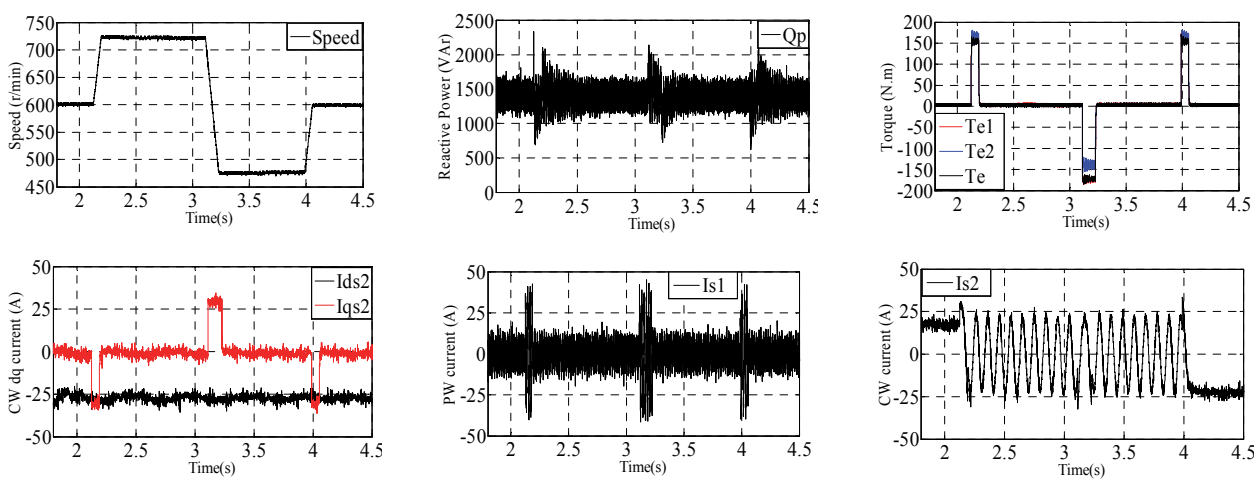

Fig. 6. Response waveforms to trapezoidal speed variations.

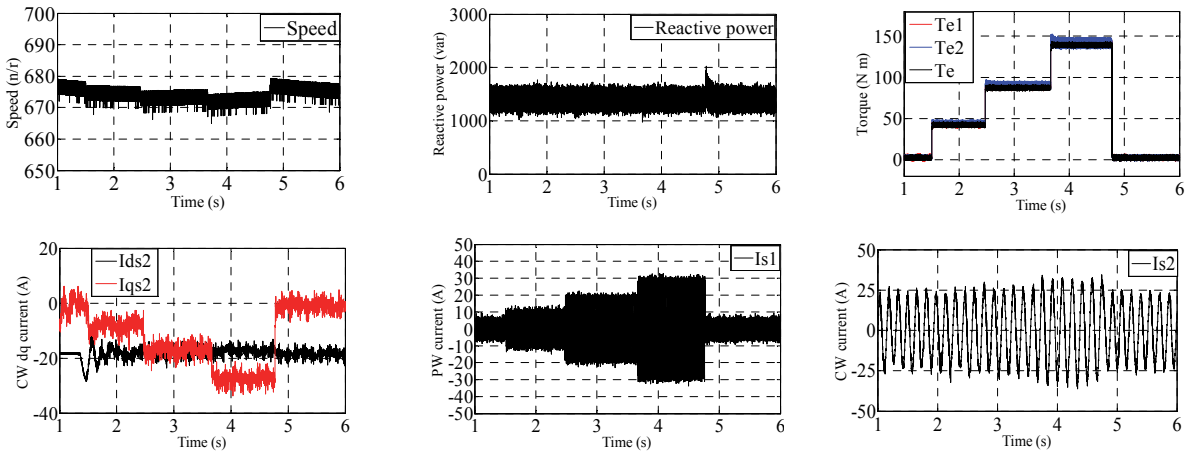

Fig. 7. Response waveforms of load torque variations.

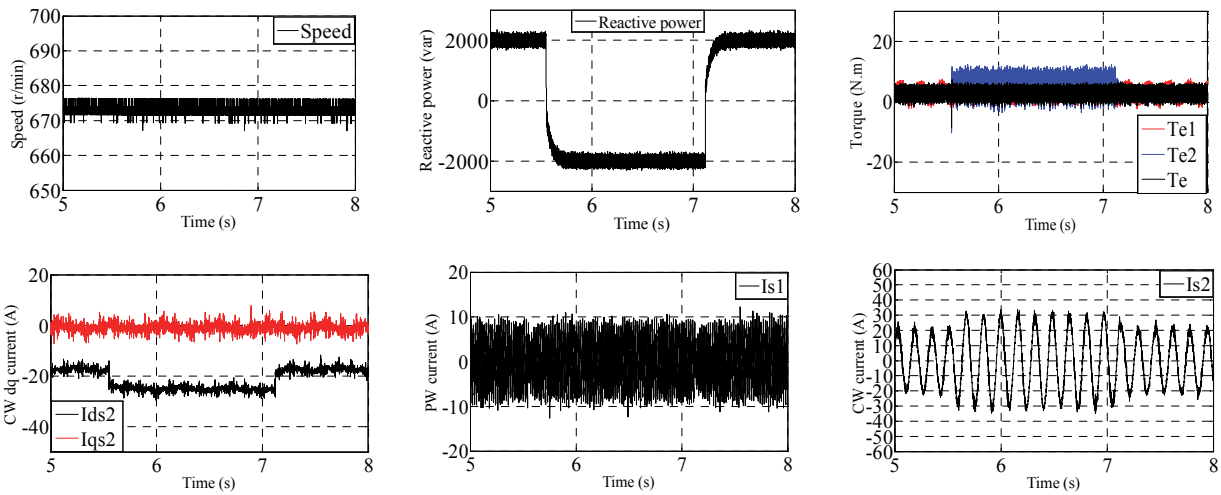

Fig. 8. Response waveforms of reactive power variations.

process, the speed is well controlled at its reference value of 674 r/min. $\bar{I}_{ds2}$ is changed to control the reactive power, and $\bar{I}_{qs2}$ is almost constant since the speed remains stable. Unlike the results of the previous section, the amplitude of the PW current remains almost constant during the dynamic process of the reactive power while the amplitude of the CW current changes from about 22 A to 31 A. This is a clear demonstration that the CW current can control the release of reactive power. Again, the calculations of T_{e1} and T_{e2} are consistent with the measured torque T_e. Experimental results illustrate that the proposed vector control strategies demonstrate good performance in controlling the reactive power, both while switching from absorbing reactive power to releasing it, and vice versa.

The obtained experimental results also indicate that the coupling effect in the reactive power control loop, i.e., Qp-$\bar{I}_{ds2}$-$\bar{V}_{ds2}$ that impacts the speed/torque control loop, i.e., ω_r-Te-$\bar{I}_{qs2}$-$\bar{V}_{qs2}$ can be significantly reduced.

V. Conclusion

This paper proposed a PW-flux-oriented generalized vector control scheme with a current hysteresis controller. A detailed theoretical analysis has been carried out to present a decoupled control method for the speed/torque and reactive power control. The control strategy was verified by experimental results showing that the controller exhibits good decoupling performance even without cross-perturbation compensation. In fact, the strongest cross-coupling effects where $\bar{V}_{ds2}$ affects the speed/torque and $\bar{V}_{qs2}$ affects the reactive power have been avoided in the proposed current hysteresis controller.

In this paper, two electromagnetic torque equations (25) and (26) for a BDFIM have been proposed based on the generalized vector model. The speed control loop has been implemented based on equation (26). The present torque expressions of the BDFIM are similar to the torque expressions of a DFIM and can facilitate the analysis of the

control methods. With the two electromagnetic torque equations, a mature control scheme for a DFIM can be applied in controlling a BDFIM more conveniently.

Since the electromagnetic torque was proposed under the condition that $\eta=\gamma=0$, in the future, a generalized electromagnetic torque equation in an arbitrary frame will be studied.

APPENDIX

$$\overline{\boldsymbol{G}}_1=\overline{\boldsymbol{C}}_4^{-1}\overline{\boldsymbol{C}}_5,\quad \overline{\boldsymbol{G}}_2=\overline{\boldsymbol{C}}_4^{-1}\overline{\boldsymbol{C}}_6,\quad G_3=C_7/L,\ \overline{\boldsymbol{G}}_4=\overline{\boldsymbol{C}}_8/C_7,$$

$$\overline{\boldsymbol{G}}_5=(\boldsymbol{I}_{N\times N}-\frac{\overline{\boldsymbol{M}}_{s2r}'}{3\overline{\boldsymbol{M}}_{s1r}(\overline{\boldsymbol{L}}_r-\overline{\boldsymbol{M}}_r)^{-1}\overline{\boldsymbol{M}}_{s2r}'}[\boldsymbol{L}\overline{\boldsymbol{C}}_8/C_7+3\overline{\boldsymbol{M}}_{s1r}(\overline{\boldsymbol{L}}_r-\overline{\boldsymbol{M}}_r)^{-1}])^{-1},$$

$$\overline{\boldsymbol{G}}_6=(\overline{\boldsymbol{L}}_r-\overline{\boldsymbol{M}}_r)^{-1}-\frac{9}{2\boldsymbol{L}_l}\overline{\boldsymbol{M}}_{s1r}'\overline{\boldsymbol{M}}_{s1r},$$

$$\overline{\boldsymbol{G}}_7=\frac{3}{2\boldsymbol{L}_l}\overline{\boldsymbol{M}}_{s1r}'+\frac{3}{2}\overline{\boldsymbol{M}}_{s2r}'(\frac{2}{9C_7\overline{\boldsymbol{M}}_{s1r}(\overline{\boldsymbol{L}}_r-\overline{\boldsymbol{M}}_r)^{-1}\overline{\boldsymbol{M}}_{s2r}'}-1),$$

$$\overline{\boldsymbol{G}}_i=[\boldsymbol{I}_{N\times N}-(\overline{\boldsymbol{G}}_1+\overline{\boldsymbol{G}}_2\overline{\boldsymbol{G}}_4)\overline{\boldsymbol{G}}_5^{-1}\overline{\boldsymbol{G}}_6]^{-1}[(\overline{\boldsymbol{G}}_1+\overline{\boldsymbol{G}}_2\overline{\boldsymbol{G}}_4)\overline{\boldsymbol{G}}_5^{-1}\overline{\boldsymbol{G}}_7+\overline{\boldsymbol{G}}_2G_3],$$

$$\overline{\boldsymbol{G}}_r=(\overline{\boldsymbol{G}}_1+\overline{\boldsymbol{G}}_2\overline{\boldsymbol{G}}_4)^{-1}(\overline{\boldsymbol{G}}_i-\overline{\boldsymbol{G}}_2G_3)$$

$$G_c=\frac{2L}{9\overline{\boldsymbol{M}}_{s1r}(\overline{\boldsymbol{L}}_r-\overline{\boldsymbol{M}}_r)^{-1}\overline{\boldsymbol{M}}_{s2r}'}[LG_3+L\overline{\boldsymbol{G}}_4\overline{\boldsymbol{G}}_r+3\overline{\boldsymbol{M}}_{s1r}(\overline{\boldsymbol{L}}_r-\overline{\boldsymbol{M}}_r)^{-1}\overline{\boldsymbol{G}}_r+3\overline{\boldsymbol{M}}_{s2r}\overline{\boldsymbol{G}}_i-1]$$

$$G_s=\frac{1}{(L_{ll}+\frac{3}{2}L_l)}\left(1-3\overline{\boldsymbol{M}}_{s1r}\overline{\boldsymbol{G}}_r\right)$$

Where:

$$C_1=\frac{C}{L},\ \overline{\boldsymbol{C}}_2=\frac{C}{L}\overline{\boldsymbol{H}}_2,\overline{\boldsymbol{C}}_3=\frac{C}{L}\overline{\boldsymbol{H}}_3,$$

$$\overline{\boldsymbol{C}}_4=\boldsymbol{I}_{N\times N}-(\overline{\boldsymbol{L}}_r-\overline{\boldsymbol{M}}_r)^{-1}\overline{\boldsymbol{M}}_{s2r}'(\overline{\boldsymbol{M}}_{s2r}')^{-1}(\overline{\boldsymbol{L}}_r-\overline{\boldsymbol{M}}_r),$$

$$\overline{\boldsymbol{C}}_5=(\overline{\boldsymbol{L}}_r-\overline{\boldsymbol{M}}_r)^{-1}[\boldsymbol{I}_{N\times N}-\overline{\boldsymbol{M}}_{s2r}'(\overline{\boldsymbol{M}}_{s2r}')^{-1}],$$

$$\overline{\boldsymbol{C}}_6=(\overline{\boldsymbol{L}}_r-\overline{\boldsymbol{M}}_r)^{-1}[\overline{\boldsymbol{M}}_{s2r}'(\overline{\boldsymbol{M}}_{s2r}')^{-1}\overline{\boldsymbol{M}}_{s1r}'-\frac{3}{2}\overline{\boldsymbol{M}}_{s1r}'],$$

$$\boldsymbol{C}_7=\boldsymbol{C}_1-\overline{\boldsymbol{C}}_3\overline{\boldsymbol{C}}_4^{-1}\overline{\boldsymbol{C}}_6,\quad \overline{\boldsymbol{C}}_8=\overline{\boldsymbol{C}}_2+\overline{\boldsymbol{C}}_3\overline{\boldsymbol{C}}_4^{-1}\overline{\boldsymbol{C}}_5.$$

Where:

$$C_1,C_7,G_3,G_c,H_1,\in constant,\ \overline{\boldsymbol{C}}_2,\overline{\boldsymbol{C}}_3,\overline{\boldsymbol{C}}_8,\overline{\boldsymbol{G}}_4\in\boldsymbol{R}^{1\times N},$$

$$\overline{\boldsymbol{C}}_6,\overline{\boldsymbol{G}}_2,\overline{\boldsymbol{G}}_7,\overline{\boldsymbol{G}}_i,\overline{\boldsymbol{G}}_r\in\boldsymbol{R}^{N\times 1},\ \overline{\boldsymbol{C}}_4,\overline{\boldsymbol{C}}_5,\overline{\boldsymbol{G}}_1,\overline{\boldsymbol{G}}_5,\overline{\boldsymbol{G}}_6\in\boldsymbol{R}^{N\times N}$$

ACKNOWLEDGMENT

The authors extend their gratitude to NSFC(61571189) and 111 project (B13009) for sponsoring this study.

REFERENCES

[1] S. Jin, L. Shi, L. Zhu, and T. Dong, "Performance comparison of direct power control for brushless doubly-fed wind power generator with different control winding structure," *IEEE Transportation Electrification Conference and Expo, Asia-Pacific*, 2016.

[2] A. L. Zhang and W. Xin, "A static two-axis model and its application in direct torque control system for brushless doubly fed induction machine," *IEEE Ninth International Conference on Power Electronics and Drive Systems*, pp. 968-973, 2011.

[3] R. Zhao, A. Zhang, Y. Ma, X. Wang, J. Yan, and Z. Ma, "The dynamic control of reactive power for the brushless doubly fed induction machine with indirect stator-quantities control scheme," *IEEE Trans. Power Electron.,* Vol. 30, No. 9, pp. 5046-5057, Oct. 2015.

[4] W. Srirattanawichaikul, S. Premrudeepreechacharn, and Y. Kumsuwan, "A comparative study of vector control strategies for rotor-side converter of DFIG wind energy systems," *International Conference on Electrical Engineering/ electronics, Computer, Telecommunications and Information Technology*, pp. 1-6, 2016.

[5] I. Sarasola, J. Poza, M. A. Rodriguez, and G. Abad, "Direct torque control for brushless doubly fed induction machines," *Electric Machines & Drives Conference, 2007. IEMDC '07. IEEE International*, pp. 1496-1501, 2007.

[6] K. Protsenko and D. Xu, "Modeling and control of brushless doubly-fed induction generators in wind energy applications," *IEEE Trans. Power Electron.,* Vol. 23, No. 3, pp. 529-535, May 2008.

[7] Y. Liu, W. Ai, B. Chen, K. Chen, and G. Luo, "Control design and experimental verification of the brushless doubly-fed machine for stand-alone power generation applications," *IET Electric Power Appl.,* Vol. 10, No. 1, pp. 25-35, Jan. 2015.

[8] X. Wang and H. Lin, "DC-link current estimation for load-side converter of brushless doubly-fed generator in the current feed-forward control," *IET Power Electron.,* Vol. 9, No. 8, pp. 1703-1710, Jun. 2016.

[9] D. Zhou and R. Spee, "Synchronous frame model and decoupled control development for doubly-fed machines," *Power Electronics Specialists Conference, Pesc '94 Record., IEEE*, Vol. 2, pp. 1229-1236, 1994.

[10] S. Shao, E. Abdi, and R. Mcmahon, "Vector control of the brushless doubly-fed machine for wind power generation," in *IEEE International Conference on Sustainable Energy Technologies*, pp. 322-327, 2008.

[11] A. K. Wallace, R. Spee, and H. K. Lauw, "Dynamic modeling of brushless doubly-fed machines," in *Industry Applications Society Meeting, 1989., Conference Record of the*, pp. 329-334 Vol. 1, 1989.

[12] R. Li, A. Wallace, R. Spee, and Y. Wang, "Two-axis model development of cage-rotor brushless doubly-fed machines," *IEEE Trans. Energy Convers.,* Vol. 6, No. 3, pp. 453-460, Sep. 1991.

[13] D. Zhou, R. Spee, G. C. Alexander, and A. K. Wallace, "A simplified method for dynamic control of brushless doubly-fed machines," *IEEE IECON International Conference on Industrial Electronics, Control, and Instrumentation*, Vol. 2, pp. 946-951, 1996.

[14] Roberts and P. Christopher, "A study of brushless doubly-fed (induction) machines: Contributions in machine analysis, design and control," *Genetics,* Vol. 148, No. 3, pp. 1353-1365, Mar. 2005.

[15] J. Poza, E. Oyarbide, D. Roye, and M. Rodriguez, "Unified reference frame dq model of the brushless doubly fed

machine," *Electric Power Applications Iee Proceedings,* Vol. 153, No. 5, pp. 726-734, Oct. 2006.
[16] J. Poza, E. Oyarbide, I. Sarasola, and M. Rodriguez, "Vector control design and experimental evaluation for the brushless doubly fed machine," *IET Electric Power Appl.,* Vol. 3, No. 4, pp. 247-256, Jul. 2009.
[17] S. Shao, E. Abdi, F. Barati, and R. Mcmahon, "Stator-flux-oriented vector control for brushless doubly fed induction generator," *IEEE Trans. Ind. Electron.,* Vol. 56, No. 10, pp. 4220-4228, Jun. 2009.
[18] F. Barati, H. Oraee, E. Abdi, and R. Mcmahon, "Derivation of a vector model for a Brushless Doubly-Fed Machine with multiple loops per nest," pp. 606-611, 2008.
[19] F. Barati, S. Shao, E. Abdi, and H. Oraee, "Generalized vector model for the brushless doubly-fed machine with a nested-loop rotor," *IEEE Trans. Ind. Electron.,* Vol. 58, No. 6, pp. 2313-2321, Aug. 2011.
[20] R. Cardenas, R. Pena, S. Alepuz, and G. Asher, "Overview of control systems for the operation of DFIGs in wind energy applications," *IEEE Trans. Ind. Electron.,* Vol. 60, No. 7, pp. 2776-2798, Jul. 2013.
[21] M. Yamamoto and O. Motoyoshi, "Active and reactive power control for doubly-fed wound rotor induction generator," *IEEE Trans. Power Electron.,* Vol. 6, No. 4, pp. 624-629, Oct. 1991.
[22] F. Barati, R. Mcmahon, S. Shao, E. Abdi, and H. Oraee, "Generalized vector control for brushless doubly fed machines with nested-loop rotor," *IEEE Trans. Ind. Electron.,* Vol. 60, No. 6, pp. 2477-2485, Jun. 2013.

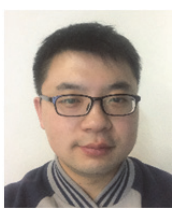

Qiwei Duan received his B.S. degree from the Shandong University of Science and Technology, Qingdao, China, in 2011. He is presently working towards his Ph.D. degree in the field of Machine Control at the North China Electric Power University, Beijing, China. His current research interests include the control of BDFIMs.

Shi Liu received the B.S. and M.S. degrees from Chongqing University, Chongqing, China; and his Ph.D. degree from the University of Cambridge, Cambridge, ENG, UK. He was a Research Professor at the Chinese Academy of Sciences, Beijing, China, in 1998; and he has been with the North China Electric Power University, Beijing, China, since 2007. His current research interests include the system integration of renewable energy and the forecast of renewable energy power generation.

H. Inaki Schlaberg obtained his M.S. degree in Real-Time Electronic Systems and his PhD from the Department of Electrical and Electronic Engineering at the University of Bradford, Bradford, ENG, UK. He was a Senior Research Fellow at the University of Leeds, Leeds, ENG, UK; a Scientific Visitor at the Chinese Academy of Sciences, Beijing, China; and is presently working as a Professor at the North China Electric Power University, Beijing, China. His current research interests include ultrasonics and electrical tomography. Professor Schlaberg is presently a Member of the IEEE Ultrasonics, Ferroelectrics, and Frequency Control Society. He has been an IEEE member since 1998.

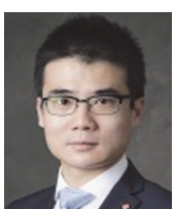

Teng Long received his Ph.D. degree in Electronics Engineering from the University of Cambridge, Cambridge, ENG, UK. He is presently working as a Lecturer at the University of Cambridge. He has held the prestigious position of being a Fellow of the Peterhouse, University of Cambridge. His current research interests include power electronics, power conversion systems, renewable energy and electric vehicles.